Structure of the KcsA Potassium Channel from *Streptomyces lividans*: A Site-Directed Spin Labeling Study of the Second Transmembrane Segment†

Adrian Gross,‡ Linda Columbus,‡ Kalman Hideg,§ Christian Altenbach,‡ and Wayne L. Hubbell*,‡

Jules Stein Eye Institute and Department of Chemistry and Biochemistry, University of California, Los Angeles, California 90095-7008, and Institute of Organic and Medicinal Chemistry, University of Pecs, Pecs, Hungary

Received April 13, 1999; Revised Manuscript Received May 28, 1999

ABSTRACT: KcsA is a prokaryotic potassium channel. The present study employs cysteine scanning mutagenesis and site-directed spin labeling to investigate the structure of the second transmembrane segment (residues 82−120) in functional tetrameric channels reconstituted in lipid bilayers. Spin−spin interactions are observed between nitroxide side chains at symmetry-related sites close to the 4-fold axis of symmetry. To aid in quantitative analysis of these interactions, a new diamagnetic analogue of the nitroxide side chain is used to prepare magnetically dilute samples with constant structure. Using constraints imposed by the spin−spin interactions, a packing model for this segment is deduced that is in excellent agreement with the recently reported crystal structure [Doyle, D., et al. (1998) *Science 280*, 69−77]. The relatively immobilized state of the nitroxide side chains suggests that the channel is rigid on the electron paramagnetic resonance time scale. Moreover, the poor sulfhydryl reactivity of the cysteine at many locations indicates that the channel is not subject to the low-frequency fluctuations that permit reaction of buried cysteines. At sites expected to be located in the pore, the accessibility of the side chains to collision with O_2 or nickel(II) ethylenediaminediacetate is low. This inaccessibility, together with the generally low mobility of the side chains throughout the sequence, makes it difficult to detect the presence of the pore based on these measurements. However, the presence of a solvated pore can be directly demonstrated using a polarity parameter deduced from the EPR spectra recorded at low temperature. These measurements also reveal the presence of a polarity gradient in the phospholipid bilayer.

Potassium channels are the phylogenetic founders of a family of proteins that facilitate the conduction of cations across membranes. Two basic structural elements of the protein are responsible for ion conduction: a water-filled pathway through the center of the protein and a finely tuned unit for ion selection. Until recently, the structure of these important proteins was elusive beyond this simple picture, mainly because there was no adequate source for the large amounts of stable and functional protein necessary for structural studies. The situation improved when it became apparent that potassium channels are ubiquitous in bacteria. The relative ease with which prokaryotic proteins can be produced allowed, for the first time, the study of potassium channels on a biochemical scale.

One channel in particular, the potassium channel KcsA from *Streptomyces lividans*, has been at the forefront of these efforts (*1*−*9*). KcsA is a small potassium channel that contains only two transmembrane segments and a pore loop, a *core domain* present in all potassium channels. KcsA can be expressed in *Escherichia coli* at high levels and, when reconstituted, exhibits the typical properties of potassium channels (*1*, *10*, *11*). Recently, a structural model of KcsA was determined on the basis of protein crystals diffracting to 3.2 Å (*4*). The model reveals that KcsA is a predominately α-helical protein assembled as a tetramer around a model-imposed 4-fold symmetry axis (Figure 1). The first transmembrane segment, TM1,[1] lies in contact with the hydrocarbon chains of the bilayer and does not participate in lining the ion pathway. The second transmembrane segment, TM2, forms a tilted inner α-helix close to the symmetry axis. A 4-fold symmetric assembly of four tilted helices results in a helical bundle, which delineates a space inside the protein shaped like an hourglass. The pore loop partially fills the larger upper cone of the hourglass, leaving a narrow pathway for ion conduction. The smaller lower cone appears to be water filled.

† This work was supported by NRSA Grant GM19007 (A.G.), NIH Grant EY05216 (W.L.H.), the Jules Stein Professorship Endowment (W.L.H.), the Bundy Foundation, and Grant 97-13 2,4/23 (K.H.) from the Hungarian Academy of Sciences.

* To whom correspondence should be addressed. Phone: (310) 206-8831. Fax: (310) 794-2144. E-mail: adrian@wlheye.jsei.ucla.edu; hubbellw@jsei.ucla.edu.

‡ University of California, Los Angeles.

§ University of Pecs.

[1] Abbreviations: CHAPS, 3-[(3-cholamidopropyl)dimethylammonio]-1-propanesulfonate; DM, *n*-dodecyl β-D-maltoside; DTT, dithiothreitol; EDTA, ethylenediaminetetraacetic acid; EPR, electron paramagnetic resonance; IPTG, isopropyl β-D-thiogalactoside; IR, infrared; LB, Luria broth; MOPS, morpholinopropanesulfonic acid; mp, melting point; NiEDDA, nickel(II) ethylenediaminediacetate; Ni−NTA, nickel(II) nitrilotriacetic acid; NMR, nuclear magnetic resonance; PMSF, phenylmethanesulfonyl fluoride; POPC, 1-palmitoyl-2-oleoyl-*sn*-glycero-3-phosphocholine; POPG, 1-palmitoyl-2-oleoyl-*sn*-glycero-3-[phospho-*rac*-(1-glycerol)]; PCR, polymerase chain reaction; R1, designation for spin-labeled side chain; SDSL, site-directed spin labeling; SDS−PAGE, sodium dodecyl sulfate−polyacrylamide gel electrophoresis; TLC, thin-layer chromatography; TM, transmembrane segment; TPX, trademark for polymethylpentene.

10.1021/bi990856k CCC: $18.00
Published on Web 07/23/1999

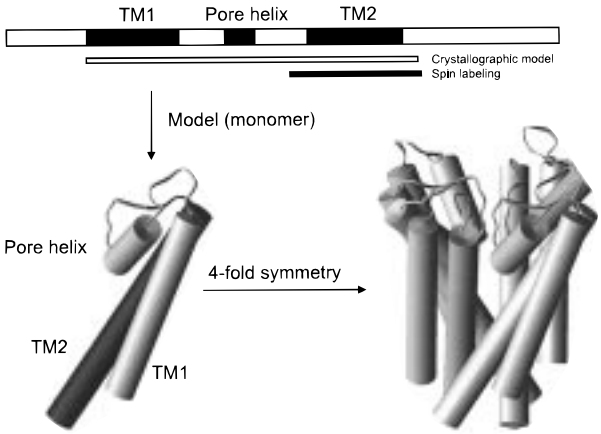

FIGURE 1: Topography of the KcsA subunit, crystallographic model, and location of spin-labeled sites. Top: Linear representation of the KcsA sequence. A subunit consists of two transmembrane segments (TM1 and TM2), a pore loop (with pore helix), and intracellular amino and carboxyl termini. The crystallographic model (*4*) covers residues 23−119, as indicated with a horizontal open bar. Site-directed spin labeling was performed between residue 82 in the extended part of the pore loop and residue 120 at the end of TM2, as indicated with a horizontal solid bar. Bottom left: Tertiary structure of a subunit. The spin-labeled region is shown in black. Bottom right: Channel assembled from four identical subunits rotated around a 4-fold axis.

In this study, we determine the structure of TM2 in the reconstituted channel using SDSL. This work, begun prior to and carried out independently of the availability of the crystal structure data, provides us with a valuable opportunity to compare and contrast the structural information obtained using these different techniques. The nitroxide side chain R1 is introduced at sites in the sequence 82−120, between the extended part of the pore loop and the end of TM2. A semiquantitative analysis of spin−spin interactions in the tetramer is used to deduce a helix packing model that is in excellent agreement with the crystal structure. To aid in the analysis, we present a new, approximately isomorphous, diamagnetic analogue of R1, designated here as R1′ (Figure 2). This analogue is used together with the paramagnetic version to obtain EPR spectra in the absence of spin−spin interaction for distance measurements. In addition, patterns of cysteine reactivity are used to infer the location of tertiary contact interactions in TM2, and these results are also in agreement with the model determined from crystallography but differ from earlier reported SDSL experiments (*8*). The channel appears to be relatively rigid as judged from cysteine reactivity and side chain mobility, a finding that seems consistent with the function of the protein.

The relative polarity of the nitroxide environment along TM2 is assessed from EPR spectra recorded in the frozen state. The polarity is periodic in sequence position along TM2, directly revealing the helical structure of the segment, the existence of a polar channel in the protein interior, and a polarity gradient in the bilayer near the protein surface. These results are particularly significant because neither side chain mobility nor accessibility to collision with paramagnetic reagents can unequivocally identify the surface of the helix in contact with the channel interior without additional assumptions regarding the structure.

The overall excellent agreement of the SDSL data with the crystallographic model indicates that the channel structure

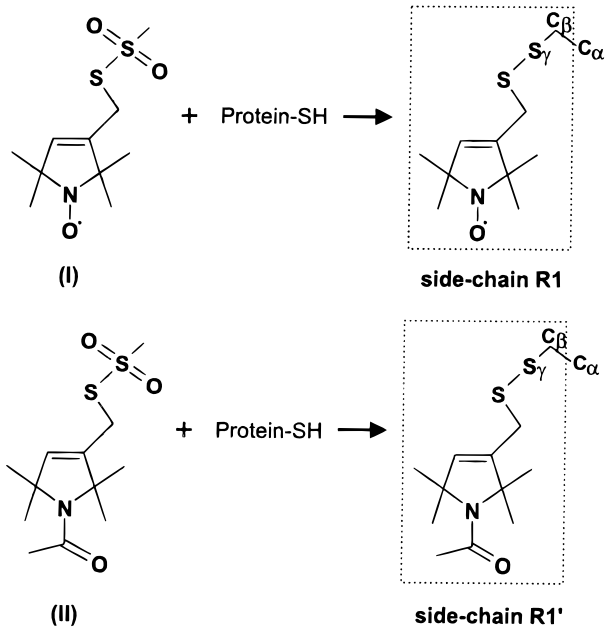

FIGURE 2: Reaction of the methanethiosulfonate reagents **I** and **II** with cysteine to generate side chains designated R1 and R1′, respectively.

is similar in the membrane and in the crystalline state, complexed with detergent. The ability of SDSL to elucidate the structure of an ion channel to the degree presented here, and to contribute valuable information unavailable by other methods, demonstrates that it is a valuable tool in the study of membrane proteins.

MATERIALS AND METHODS

Labeling Reagents (Figure 2). Methanethiosulfonate reagent **I** was prepared as described (*12*). A diamagnetic analogue of reagent **I** was prepared according to the scheme

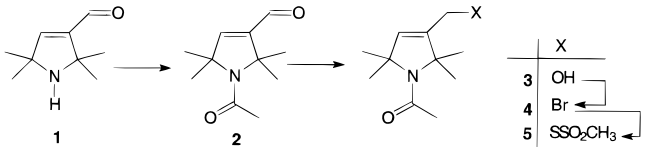

Compound **1** was prepared according to published procedures (*13*). To a mixture of compound **1** (1.53 g, 10.0 mmol) and Et_3N (1.11 g, 11.0 mmol) in CH_2Cl_2 (30 mL) was added dropwise acetyl chloride (863 mg, 11.0 mmol) at 0 °C. The mixture was allowed to warm to room temperature and stirred for 1 h. Methanol (1 mL) was then added, and the mixture was stirred for 5 min to remove traces of acetyl chloride. The solvents were evaporated, the residue was dissolved in brine (10 mL) and extracted with $CHCl_3$ (2 × 15 mL), and the organic phase was separated, dried ($MgSO_4$), and filtered. The filtrate was evaporated in vacuo, and the residue was crystallized from hexane to give 1.10 g of **2** as a white solid (52%). Analytical data: mp 95−97 °C; R_f 0.43 ($CHCl_3$/Et_2O, 2:1); IR (Nujol) 1690, 1640, 1600 cm^{-1}; ^1H NMR (400 MHz, $CDCl_3$), δ 1.63 (s, 6H), 1.66 (s, 6H), 2.19 (s, 3H), 6.49 (s, 1H), 9.61 (s, 1H).

To a stirred solution of compound **2** (975 mg, 5.0 mmol) in EtOH (25 mL) was added $NaBH_4$ (378 mg, 10.0 mmol), and the mixture was stirred for an additional 30 min. The EtOH was evaporated, and the residue was dissolved in H_2O (10 mL). The aqueous solution was extracted with $CHCl_3$

(2 × 15 mL), and the organic phase was separated, dried ($MgSO_4$), and filtered. The filtrate was evaporated in vacuo, and the residue was crystallized from hexane/Et_2O to give 768 mg of alcohol **3** as a white solid (78%). Analytical data: mp 107−109 °C; R_f 0.20 ($CHCl_3$/Et_2O, 2:1); IR (Nujol) 3240, 1590 cm^{-1}; ^1H NMR (400 MHz, $CDCl_3$) δ 1.47 (s, 3H), 1.50 (s, 3H), 1.54 (s, 6H), 2.15 (s, 3H), 4.19 (s, 2H), 5.36 (s, 1H).

To a stirred solution of alcohol **3** (985 mg, 5.0 mmol) and Et_3N (606 mg, 6.0 mmol) in CH_2Cl_2 (20 mL) was added dropwise methanesulfonyl chloride (687 mg, 6.0 mmol) at 0 °C, and the mixture was stirred at room temperature for 1 h. The organic phase was washed with brine (10 mL), separated, dried ($MgSO_4$), and filtered, and the filtrate was evaporated to dryness. The residue was immediately dissolved in anhydrous acetone (20 mL), LiBr (868 mg, 10.0 mmol) was added, and the mixture was stirred and refluxed for 30 min. The acetone was evaporated, the residue was dissolved in brine (15 mL), and the solution was extracted with EtOAc (2 × 20 mL). The organic phase was separated, dried ($MgSO_4$), and filtered, and the solvent was evaporated. The residue was purified by flash column chromatography (hexane/EtOAc) to give 683 mg of bromide **4** as a thick pale yellow oil (53%). Analytical data: R_f 0.56 ($CHCl_3$/Et_2O, 2:1); IR (neat) 1600 cm^{-1}; ^1H NMR (400 MHz, $CDCl_3$) δ 1.49 (s, 3H), 1.51 (s, 3H), 1.57 (s, 6H), 2.26 (s, 3H), 4.02 (s, 2H), 5.52 (s, 1H).

A mixture of bromide **4** (520 mg, 2.0 mmol) and $NaSSO_2$-CH_3 (536 mg, 4.0 mmol) in EtOH (15 mL) and water (5 mL) was refluxed for 30 min. The solvents were evaporated, the residue was dissolved in brine (10 mL), and the solution was extracted with $CHCl_3$ (2 × 15 mL). The $CHCl_3$ solution was dried ($MgSO_4$) and filtered, and the solvent was evaporated. The residue was purified by flash column chromatography ($CHCl_3$/Et_2O) to give 262 mg of methanethiosulfonate **5** (45%). Analytical data: mp 111−113 °C; R_f 0.25 ($CHCl_3$/Et_2O, 2:1); IR (Nujol) 1600 cm^{-1}; ^1H NMR (400 MHz, $CDCl_3$) δ 1.48 (s, 6H), 1.58 (s, 6H), 2.17 (s, 3H), 3.31 (s, 3H), 3.79 (s, 2H), 5.52 (s, 1H).

Melting points are uncorrected. Flash column chromatography was performed on Merck Kieselgel 60 (0.040−0.063 mm). Qualitative TLC was carried out on commercially prepared plates (20 × 20 × 0.02 cm) coated with Merck Kieselgel GF_{254}, and spots were visualized in I_2 vapor.

Preparation and Expression of Cysteine Substitution Mutants. KcsA was recloned by PCR from *S. lividans* using Pfu polymerase (Stratagene, La Jolla, CA); the fragment was sequenced on both strands and subcloned into the pQE32 expression vector (Qiagen, Chatsworth, CA). This construct introduced the sequence MRGSHHHHHHGIR at the amino terminus of KcsA (*1*). Cysteine mutants were generated by PCR cassette mutagenesis and verified by sequencing the insert on both strands. The various cysteine substitution mutants and their spin-labeled derivatives are designated by giving the original residue, the amino acid number, and the new residue, in that order. *E. coli* (Novablue, Novagen, Madison, WI) were transformed and grown to logarithmic phase in 1 L of LB, induced with 0.5 mM IPTG, and cultured for 90 min. Cells were harvested by centrifugation, washed, and resuspended in lysis buffer (20 mM MOPS, 140 mM NaCl, 10 mM KCl, 10 mM EDTA, pH 6.7), supplemented with 5 mM DTT and protease inhibitors (2.5 μg/mL aprotinin, 1 μg/mL leupeptin, and 0.4 mg/mL PMSF). Cells were disrupted in a French press, and the membrane fraction was obtained by ultracentrifugation. The membrane pellet was solubilized at room temperature in the same buffer with 20 mM dodecyl maltoside (DM) for 30 min, and the solution was cleared by ultracentrifugation.

Protein Purification and Spin Labeling. Crude KcsA solubilized in DM was bound to a cation-exchange chromatography resin (Resource S, Pharmacia, Piscataway, NJ) under low ionic strength conditions (20 mM MOPS, 10 mM KCl, 2 mM EDTA, 1 mM DM, pH 6.7). The adsorbed protein was eluted with a linear gradient formed from the above buffer and 350 mM Na_2SO_4. About a 10-fold molar excess of spin label was added to the partially purified channel, and the reaction was incubated overnight in the dark at room temperature. Unreacted label and EDTA were removed by gel filtration (Sephadex G-25, Pharmacia, Piscataway, NJ) prior to loading the sample on Ni−NTA Superose (Qiagen, Chatsworth, CA). With KcsA immobilized on the resin, the detergent was exchanged to 10 mM CHAPS, and the protein was eluted with a step gradient from 50 to 500 mM imidazole. The yield for the purified wild-type channel was approximately 1 mg/L of culture.

Reconstitution and EPR Measurements. KcsA was reconstituted in a 4:1 molar mixture of POPC/POPG (Avanti Polar, Alabaster, AL) by gel filtration on Sephadex G-25 (Pharmacia, Piscataway, NJ) following the method of Green and Bell (*14*). The molar protein-to-lipid ratio was about 1:1000, and the solution contained 20 mM MOPS, 140 mM NaCl, 10 mM KCl, and 0.02% NaN_3, pH 6.7. To establish that the wild-type channel is functional under the chosen conditions, liposomes containing wild-type KcsA were assayed for channel function with a standard ^{86}Rb influx assay with valinomycin (*15*). The vesicle size was determined by transmission electron microscopy (*16*).

Vesicles containing spin-labeled KcsA were concentrated by ultrafiltration (Amicon, Beverly, MA) or ultracentrifugation and loaded into gas-permeable TPX capillaries for measurements at room temperature or into quartz capillaries for measurements in frozen solution. First derivative absorption spectra were measured on an X-band Varian E-109 spectrometer fitted with a loop-gap resonator (*17*). Spectra were recorded at either 100 or 200 G scan widths. All 100 G scans were acquired under field-frequency lock. The incident microwave power was 2 mW and 0.5 mW for measurements at room temperature and −20 °C, respectively. The approximate amount of protein in a sample was determined by quantitative amino acid analysis. The number of spins in the same sample was determined from the second integral of the spectrum referenced to a known standard.

Side chain accessibility was determined for molecular oxygen in equilibrium with air and for 20 mM NiEDDA. NiEDDA is relatively membrane impermeable and thus does not have access to the interior volume of lipid vesicles, as judged by the method of Vistnes and Puskin (*18*). However, after two cycles of freeze−thaw treatment, the reagent is distributed through all compartments in the system. In the experiments reported here, five cycles of freeze−thaw were used to ensure access of NiEDDA to the vesicle interior. For samples showing evidence of spin−spin interaction, the measurement was made on channels labeled with a mixture of R1 and R1′ where spin−spin interactions were negligible.

The accessibility parameter Π was measured by power saturation of the first derivative $M_i = 0$ line (*19*), and other measurements were as described in the text.

Simulation of Dipolar-Broadened Spectra. For EPR spectra that showed broadening due to dipolar interaction with a neighboring nitroxide, the spectra were simulated by convolution methods (*20*, *21*). In the implementation presented here, the EPR spectrum for R1 at a particular site in the absence of dipolar interaction was obtained by labeling the corresponding cysteine mutant with a mixture of labels **I** and **II** (1:4 mole ratio). The spectrum was convoluted with a broadening function to generate the dipolar-broadened spectrum. The broadening function was a sum of Pake functions (*22*) representing a set of distances normally distributed about a mean. To account for the presence of a noninteracting component due to incomplete labeling, the central value of this sum is adjusted before convolution.

RESULTS

Labeling Yield Limits the Sites That Can Be Studied by SDSL. Thirty-nine single cysteine substitution mutants in the second transmembrane segment of KcsA spanning residues Y82 and E120 were prepared for spin labeling. The various mutants yielded ≈1 mg of purified protein/L of culture, except for P83C, V84C, T85C, G88C, and R89C, which expressed poorly relative to the others, yielding <0.1 mg/L of culture. KcsA contains no native cysteine residues, and therefore, it should not react with the thiol-specific methanethiosulfonate reagent **I** (Figure 2). However, following a single-step nickel affinity purification, which provided protein of ≈95% purity, the wild-type channel had an EPR signal corresponding to ≈0.05−0.1 spin per monomer (Figure 3, background spectrum). In an attempt to eliminate this background signal, an ion-exchange chromatographic step was introduced preceding the nickel affinity step, as described in Materials and Methods. This step alone provided protein of ≈95% purity, and the sequential chromatographic procedures gave a purity estimated to be >99% based on amino acid sequencing, total amino acid analysis, and SDS−PAGE (data not shown). Despite the additional purification step, the small background signal remained, and its origin is unknown. In most instances, this background signal does not impede the interpretation of the data, because the EPR signal from the spin label at the desired site overwhelms the background. However, at several sites in TM2, the extent of labeling was low (≈5−10%) and the recorded EPR spectra were similar to that of the background (Table 1).

Although valuable information about a protein can often be obtained by labeling a few individual residues, nitroxide scanning requires continuous specific labeling throughout a given segment. For the second transmembrane segment of KcsA, all residues between V106 and E120, except A111, show labeling above background (Table 1). In contrast, labeling between residues Y82 and L105 is sporadic and to some extent periodic in occurrence (see Discussion). Figure 3 shows the normalized EPR spectra of R1 introduced at each site between residues Y82 and E120, except for those that had both poor labeling and EPR spectra similar to background. For sites with spectra distinct from background, the extent of labeling was estimated to fall in the range of 15−50%. The spectra shown in Figure 3A were recorded at

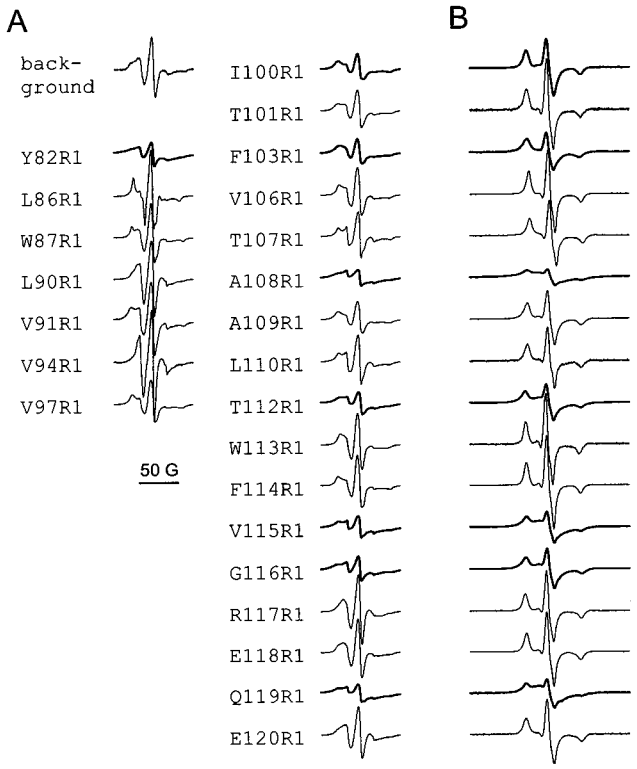

FIGURE 3: First derivative absorption EPR spectra of R1 mutant channels reconstituted in liposomes. Spectra in bold show evidence of line broadening due to spin−spin interaction. (A) Spectra were acquired at room temperature over a scan width of 100 G. Only mutants with spectra distinct from background are shown (see text). Spectra are normalized to reflect approximately equal numbers of spin. (B) Spectra were acquired at −20 °C over 200 G for mutants I100 to E120. Spectra are normalized to reflect approximately equal numbers of spin.

room temperature, while those in Figure 3B were recorded in frozen solution at −20 °C in order to evaluate static dipolar interactions and effects of polarity (see below).

Spin−Spin Interactions Lead to Spectral Broadening. A notable feature of the spectra in Figure 3 is a marked broadening of the resonance lines at positions 82, 100, 103, 108, 112, 115, 116, and 119 (bold traces), resulting in a lower relative intensity in the normalized spectra. Such broadening may be indicative of spin−spin interactions, which are expected at sites that lie near the symmetry axis of the tetramer. The notion that the spectral broadening is due to spin−spin interaction can be tested. If this were the case, a reduction of the number of spins per tetramer would decrease the extent of broadening of the spectrum. Such a reduction in the number of spins per channel should ideally be achieved without altering the immediate environment surrounding the remaining spin label. The idea is to abolish the magnetic interaction but not other structural perturbations that may be caused by the close proximity of other labels. This is best achieved by reacting the channel with a mixture of two approximately isosteric labels, one paramagnetic and one diamagnetic (Figure 2). An additional advantage of this approach is that the degree of spin underlabeling can be controlled. Given equal reactivity of the two labels, a valid assumption given their comparable size and identical sulfhydryl chemistry, the reaction leads to a binomial distribution of labels on channels.

Table 1: Labeling Yields of Cysteine Mutants[a]

mutant	yield	mutant	yield
background	*	T101C	**
Y82C	**	S102C	*
P83C	[*]	F103C	**
V84C	[*]	G104C	*
T85C	[*]	L105C	*
L86C	**	V106C	**
W87C	**	T107C	**
G88C	[*]	A108C	**
R89C	[**]	A109C	**
L90C	**	L110C	**
V91C	**	A111C	*
A92C	*	T112C	**
V93C	*	W113C	**
V94C	**	F114C	**
V95C	*	V115C	**
M96C	*	G116C	**
V97C	**	R117C	**
A98C	*	E118C	**
G99C	*	Q119C	**
I100C	**	E120C	**

[a] The labeling yield, the fraction of monomers bearing a spin label in a given sample, was estimated from amino acid analysis and double integration of the EPR spectrum, as described in Materials and Methods. Due to the large errors inherent in these procedures, especially for small sample sizes, the computed labeling yield is considered to be only a qualitative measure. Thus, results are categorized simply as poor (*) or adequate (**) labeling sites. Poorly labeled sites are those that had estimated labeling yields ≤ 0.1 and had EPR spectra essentially identical to background (see text). Adequately labeled sites have yields > 0.1 and have unique EPR spectra. Brackets indicate mutants with low protein yield (< 0.1 mg/L of culture). Key: [ ], poor protein expression (< 0.1 mg/L). *, poor labeling ($\leq 10\%$); spectrum similar to background. **, adequate labeling ($> 10\%$); distinct spectrum.

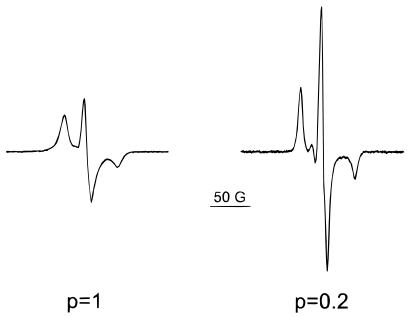

FIGURE 4: Dilution of the magnetic interaction. F103C mutant channels were reacted with reagent **I** (left) and a mixture of reagents **I** and **II** (right). The *p* value indicates the fraction of paramagnetic label in the mixture. The spectra were acquired at −20 °C. The scan width is 200 G, and the spectra are normalized to approximately equal numbers of spins.

Figure 4 shows a representative experiment where the F103C mutant was labeled with mixtures of labels **I** (paramagnetic) and **II** (diamagnetic). The *p* value refers to the fraction of the paramagnetic label in the applied mixture. At $p = 1$, all labels are paramagnetic, whereas at $p = 0.2$, every fifth label is paramagnetic. The data demonstrate that as the number of spins per channel molecule is reduced, the spectrum changes to reflect a reduction in spin−spin interaction. Given the assumption of a binomial distribution of labels, a majority of labeled channels has only one paramagnetic label at a fractional labeling of 0.2. Therefore, this technique can reveal an approximate spectrum of a fully labeled channel without the broadening due to spin−spin interactions. The spin dilution experiment demonstrates that spin−spin interaction must be the operating broadening mechanism.

The sites with prominent spin−spin interaction must be those close to the symmetry axis of the tetramer, facing the lumen of the channel. Molecular modeling based on the crystal structure of the channel indicates that it is not possible to accommodate more than a maximum of two R1 side chains in the channel lumen at the sites for which spin−spin interaction is detected. This is consistent with our labeling yield of ≈20−40% for cysteine mutants at channel lumen sites. Thus, it is reasonable to assume that the maximum number of interacting spins per channel tetramer is 2.

In frozen solution, the static magnetic dipole−dipole interactions between pairs of nitroxides can be used to estimate interspin distances by an empirical method, by spectral simulation, or by deconvolution methods (*20*, *21*, *23*, *24*). Here we employ both an empirical and a simulation method. In the empirical method of Kokorin (*23*), an amplitude ratio, $d1/d$ (Figure 5), is calibrated as a function of interspin distance using frozen solutions of nitroxides with a known distribution of interspin distances or using simulated spectra. For noninteracting spins, $d1/d \approx 0.35$ as determined from both simulated and experimental spectra. The larger this ratio, the stronger the dipolar interaction between two nitroxides and the closer they are in space. In the case of the labeled channel, there is likely to be a significant amount of monolabeled protein, and the $d1/d$ ratio will underestimate the spin−spin interaction and overestimate the interspin distance.[2] Figure 5A shows a plot of $d1/d$ as a function of amino acid position. The relationship is periodic, and the same residues with broadened spectra at room temperature also show large values of $d1/d$ and, hence, short interspin distances. In all cases, the interaction is reduced when the mutant channel is labeled with a mixture of reagents **I** and **II** ($p = 0.2$, open symbols).

For simulation of spectra showing spin−spin interaction, a magnetically dilute spectrum is convoluted with a broadening function to generate a simulated interacting spectrum (see Materials and Methods). In an iterative process, the broadening function is adjusted to fit the simulated spectrum to the experimental spectrum. The EPR absorption spectra for the interacting spin pairs and the corresponding simulated spectra (dashed lines) are shown in Figure 5B, along with the average and range of the interspin distance. The absorption spectra are shown because the relative overall breadths of the spectra, the relevant quantity for spin−spin interaction, are more easily appreciated. The longest distances of 17 and 14 Å occur at I100R1 and F103R1, respectively, while the remaining spin pairs lie in the range of 9−11 Å, the shortest being at A108R1. Both methods for distance determination give results that are generally consistent with the crystal structure, as shown in Figure 5A (dashed line).

A Model of TM2 Assembly Based on Spin−Spin Interactions. The period of the occurrence of spin−spin interactions,

[2] The effect of monolabeled protein on the $d1/d$ ratio was investigated by simulation of spectra for interacting spin pairs with variable amounts of noninteracting spin as background. The results indicate that the error in the $d1/d$ ratio increases with increasing amounts of monolabeled protein and decreases with distance. For the extreme case where half the spin labels are in monolabeled proteins, the error is 20% at 12 Å and 4% at 20 Å.

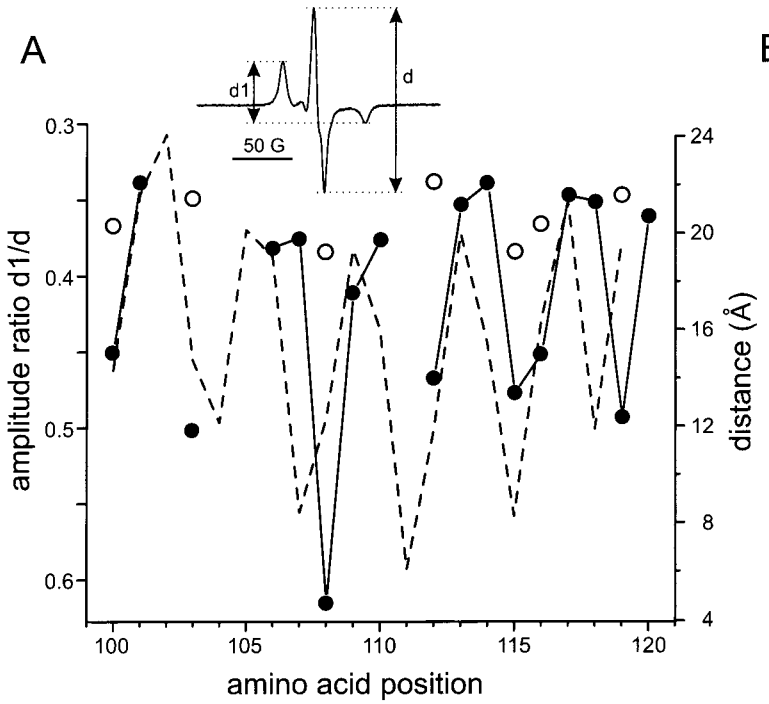

FIGURE 5: Magnetic dipolar interaction between symmetry-related nitroxides. (A) Left axis: $d1/d$ amplitude ratio as a function of amino acid position (solid line) between I100 and E120. Note that the axis is inverted for comparison with distances in the crystal structure. The amplitudes $d1$ and d are defined in the inset. Symbols: filled circles, labeling at $p = 1$; open circles, labeling at $p = 0.2$. Inset: spectrum of F103R1 ($p = 0.2$) acquired over 200 G at −20 °C. Right axis: distances in the crystal structure (dashed line) between symmetry-related amino acids on diagonal subunits measured at the C_β position (C_α for G104 and G116). Residue E120 was not modeled in the crystal structure. (B) Absorption spectra for the interacting spin pairs in frozen solution (solid lines) and simulated spectra (dashed lines) with an average interspin distance and range as indicated, see Materials and Methods. The scan width was 200 G.

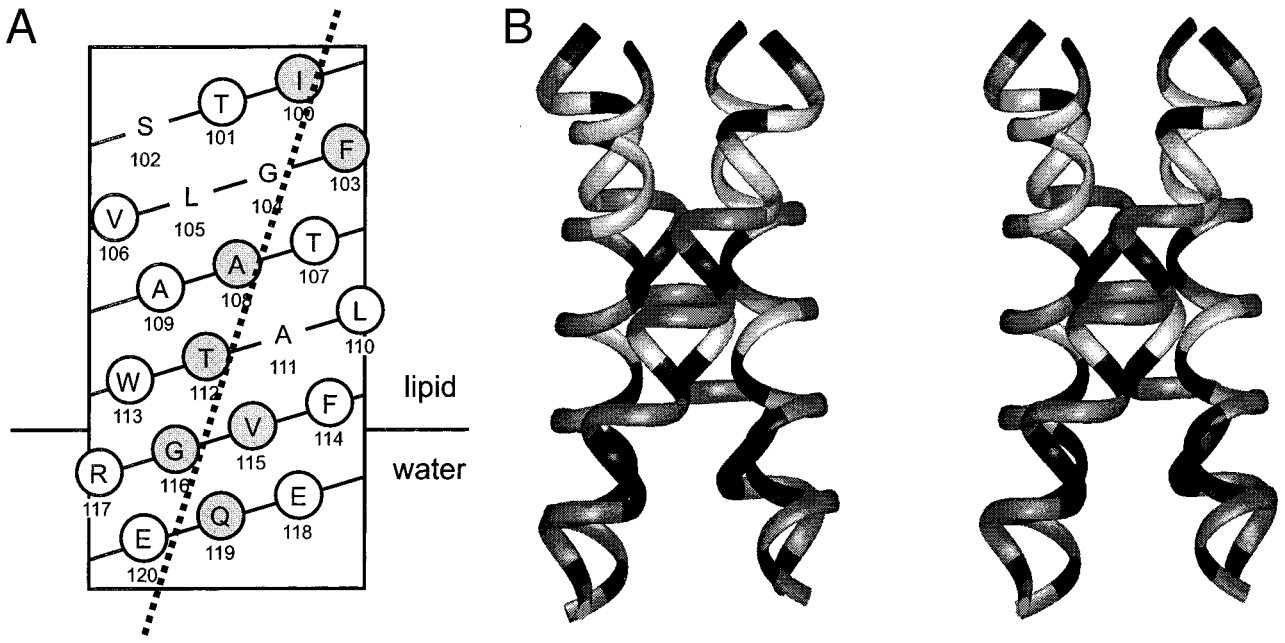

FIGURE 6: Dipolar interaction as a structural constraint. (A) Helical net representation of TM2 between I100 and E120. Symbols: filled circles, residues with dipolar interaction; open circles, residues without evidence of dipolar interaction. A dotted line is drawn through the interacting residues to support the eye. The location of the water−lipid interface is indicated as determined by collision data presented in Figure 7A. (B) Backbone ribbon model of four TM2 helices arranged around a 4-fold symmetry axis. The helices are tilted to the left with respect to the symmetry axis and cross each other at position A108. Key: black areas, dipolar interaction; gray areas, no dipolar interaction; white areas, poor labeling.

every third or fourth residue, reveals the α-helical secondary structure. Moreover, the spin−spin interaction orients the α-helix with respect to the symmetry axis because interacting residues must face this axis. Similarly, we can conclude that the helix must run roughly parallel to the symmetry axis since there is an interacting residue at every turn of the helix. Figure 6A shows the same qualitative data in a helical representation to highlight the relative position of residues along a regular helix. Residues with identified spin−spin interactions are shown as filled circles. Although the interact-

ing residues are clearly aligned, they are not aligned straight along the helix but curve around it, as indicated by the dotted line. Since the interacting residues must remain close to the symmetry axis, this axis must be tilted with respect to the helix. If we assume that the symmetry axis is normal to the bilayer, the helices in the assembled helical bundle would have a slight leftward tilt with respect to the membrane normal.

To generate a model for TM2 helix packing, the helix in Figure 6A is carried through a 4-fold rotation. Before this is done, however, the location of the rotation axis with respect to the helix must be specified. The lateral placement determines where the bundle is narrowest, and finding this point is thus equivalent to determining the position of closest approach along the length of the helix. According to the data presented in Figure 5, the strongest spin−spin interaction between the helices occurs around position A108. The pathway through the helical bundle is thus narrowest at this position. Figure 6B shows a model of four TM2 helices assembled around a 4-fold axis using these constraints. The helices are oriented to project interacting residues toward the symmetry axis, are tilted to the left with respect to the axis, and cross each other at position A108. These conclusions, based solely on spin−spin interaction data, are consistent with the crystal structure. It is worth noting that a spin−spin interaction is also observed at position Y82, indicating proximity of site 82 to the symmetry axis (Figure 3A). Residue Y82 in KcsA corresponds to residue T449 in the Shaker potassium channel, the first residue of a potassium channel shown to lie very close to the symmetry axis (*25*).

The Lumen of the Channel Is Inaccessible to Colliders. Tertiary interactions and topography of helices in membrane proteins are often revealed by the accessibility of the R1 residues to collision with polar (NiEDDA) and nonpolar (O_2) paramagnetic reagents (*26*, *27*). Figure 7A shows the accessibility parameters $\Pi(O_2)$ and Π(NiEDDA) for R1 along the sequence 100−120 in the TM2 helix. Although some points are missing due to poor labeling, it is apparent that the variation of $\Pi(O_2)$ with position is consistent with a helical periodicity. The sites expected to face the channel lumen within the transmembrane region, based on spin−spin interaction, lie at or near the local minima in $\Pi(O_2)$ with values from 0.1 to 0.2. For reference, R1 at buried sites, water-exposed sites, and lipid-exposed sites have $\Pi(O_2)$ ≈0.05, ≈0.45−0.55, and ≈1, respectively (*27*−*29* and Altenbach and Hubbell, unpublished observation). Thus, it is apparent that residues in the channel interior are inaccessible to molecular oxygen, relative to water-exposed sites. The maximum value of $\Pi(O_2)$, observed at T101R1 and G116R1, is ≈0.32. Possible topological locations for these two sites will be discussed below.

Values of Π(NiEDDA) are very low throughout the sequence 100−115, the maximum being ≈0.2 at T112R1. For reference, in 20 mM NiEDDA, R1 sites exposed to water or lipid or buried in a protein interior have Π(NiEDDA) ≈6, <0.1, and 0.01, respectively (*27*−*29* and Altenbach and Hubbell, unpublished observation). Thus, sites in the channel interior are inaccessible to NiEDDA as well as to O_2. The sharp increase in Π(NiEDDA) between residues W113 and R117, both of which face away from the pore, indicates that between these two residues the helix is crossing the lipid−water interface. Therefore, the last residues projecting into the bilayer are the aromatic residues W113 and F114. It has been found in other membrane proteins that aromatic residues are often located at the lipid−water interface (*30*−*33*).

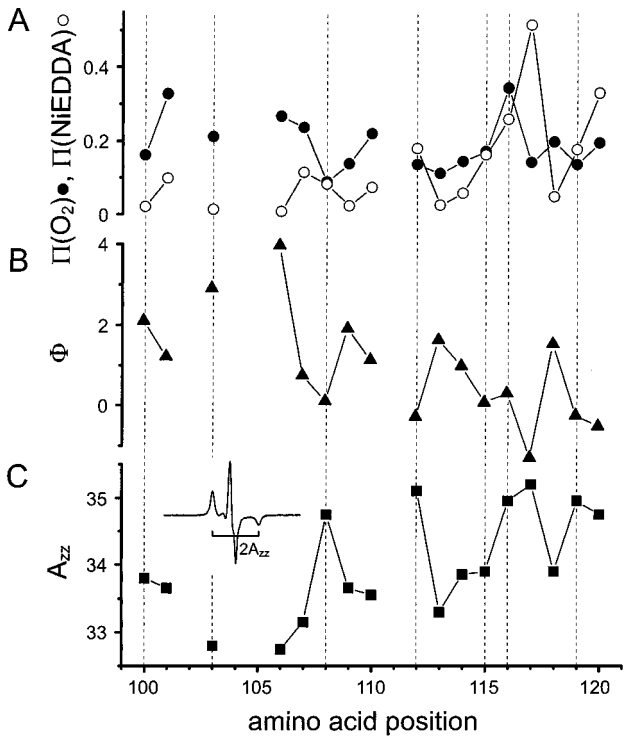

FIGURE 7: Topography of the TM2 helix between residues 100 and 120. Dashed vertical lines mark the positions of interacting residues. (A) Accessibility parameter Π for oxygen in equilibrium with air (solid circles) and 20 mM NiEDDA (open circles) as a function of sequence position. (B) Φ (triangles) as a function of sequence position. Φ was calculated from the data in (A) [$\Phi = \ln[\Pi(O_2)/\Pi(\text{NiEDDA})]$]. (C) A_{zz} (squares) as a function of sequence position. $2A_{zz}$ was measured from low-temperature spectra as shown in the inset. The inset shows the spectrum of F103R1 ($p = 0.2$) at −20 °C acquired over 200 G.

To identify lipid-facing residues on helices in membrane proteins, the function $\Phi = \ln[\Pi(O_2)/\Pi(\text{NiEDDA})]$ has been employed (*27*). Lipid-facing residues have a relatively high $\Pi(O_2)$ and a low Π(NiEDDA) due to the differential solubility of the reagents in the bilayer interior. The ratio of the accessibility parameters is used to reduce the effect of steric factors and to provide a value proportional to the simple concentration ratio of the reagents in the immediate environment of R1 (*28*). Thus, Φ will be at or near a local maximum for sites exposed to the bilayer interior. The absolute values of these local maxima vary with the depth of the residue in the bilayer (*28*). Figure 7B shows a plot of Φ for residues in the sequence 100−120. In the segment 100−105, the data are too incomplete to identify local maxima. The data are nearly continuous for the remaining segment, and well-resolved local maxima can be identified at positions 106 (likely), 109, 113, 116 (weak), and 118. In addition, residues L110R1 and F114R1 are close enough to their local maxima to be counted as potential lipid-facing residues. Further evidence for these assignments is given below.

Measurement of Local Polarity around R1. Because of the inaccessibility of the lumen interior to either O_2 or NiEDDA, accessibility measurements cannot directly reveal the presence of an aqueous channel in the protein interior. However, the aqueous lumen should be directly reflected in

the polarity of the R1 environment. The elements of the nitroxide hyperfine (A) and *g*-factor (*g*) tensors are both sensitive measures of solvent polarity (dielectric constant) (*34*). In the absence of motion in frozen solution, the principal value of the hyperfine tensor (A_{zz}) is readily measured through the splitting of the outer hyperfine extrema ($2A_{zz}$; Figure 7C, inset). The value of A_{zz} for R1 ranges from ≈32 G in a hydrocarbon solvent to ≈37 G in bulk water.[3] Figure 7C shows a plot of A_{zz} as a function of sequence position in the region from 100 to 120. As is evident, the effective polarity around the R1 side chains varies periodically with position in the sequence 106−120. With the exception of V115, the interacting residues (dashed vertical lines in Figure 7) occur at local maxima in polarity, consistent with their exposure to a polar environment. Interestingly, the values at these maxima increase toward greater polarity along the helix, and both minima and maxima increase almost in parallel. Outside the membrane, from about V115 on, the polarity is generally high with the notable exception of residue E118. For the segment from 100 to 105, the data are incomplete, and no conclusions can be drawn regarding periodicity. However, R1 at position 103, an interaction site, is in a region of very low polarity and cannot be at a local maximum (see Discussion). The data of Figure 7C support the assignment of lipid-facing residues as those at the maxima in Φ (Figure 7B). Clearly, the maxima in Φ occur close to minima in A_{zz}, i.e., at minima in the local polarity.

Mobility Gradient of R1 along TM2. The mobility of the R1 side chain, reflected in the shape of the EPR spectrum, is strongly correlated with its location in the tertiary fold of a protein. Thus, the EPR spectrum of an R1 residue has been shown to resolve helix surface sites, loop sites, tertiary contact sites, and buried sites in T4 lysozyme (*35*). An examination of the EPR spectra in Figure 3A reveals that, in the sequence 100−116, all R1 residues are relatively immobilized, judging from the resolved outer hyperfine extrema. This includes the lumen-facing residues with spin−spin interaction, where the mobility is more clearly revealed in the noninteracting line shape of magnetically diluted samples (data not shown). This result is consistent with the inaccessibility of the lumen to both O_2 and NiEDDA. Interestingly, the residues facing the lipid bilayer as judged by Φ and A_{zz} values are among the immobilized set (V106, A109, L110, W113, and F114). Figure 8 shows a comparison of the spectra from V106R1, L110R1, and W113R1 from the KcsA channel with those from helix surface sites in T4 lysozyme (D72R1) and bacteriorhodopsin (V124R1). The latter two spectra were selected to represent the most highly restricted helix surface sites in those proteins. As can be seen, the spectra from the KcsA sites reflect an even higher degree of immobilization. The mobility of the R1 side chains increases dramatically where the TM2 helix crosses from the membrane interior to the aqueous phase. Thus residues R117R1, E118R1, and E120R1 have spectra that reflect a relatively high mobility compared to their counterparts in the transbilayer sequence. A similar mobility gradient along a helix as it crosses from the membrane to water has been observed in rhodopsin (*29*).

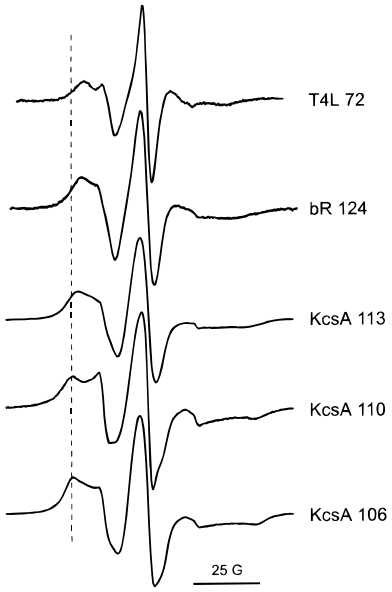

FIGURE 8: Comparison of selected EPR spectra for R1 residues located on the outer surface of helices in proteins of known structure. Residue D72R1 in T4 lysozyme is one of the most motionally restricted helix surface sites in the protein (*35*). Residue V124R1 in bacteriorhodopsin is located on the lipid-facing surface of transmembrane helix D (*28*). The KcsA spectra are taken from Figure 3. The vertical dashed line is drawn to support the eye in comparing the positions of resolved outer resonance peaks. The spectra are ranked according to apparent mobility of R1.

DISCUSSION

Spin−Spin Interaction as a Structural Constraint. Elucidating protein structure with SDSL is generally a two-step process. First, the secondary structure of a region is identified through periodic variations in the EPR data. Such an assessment is always possible if the region of interest resides in an asymmetric environment. In this study, we present a new approach to detecting this asymmetry. In a second step, the secondary structural elements are assembled into a tertiary structure by distance measurements between residues based on spin−spin interactions. In KcsA, it is possible to build a model of the TM2 segment in the tetramer based on a single form of constraint: the strength of spin−spin interactions. These interactions identify the nature of the underlying secondary structure and its orientation, as well as determine how the secondary structural elements assemble (Figure 6). This situation is a direct consequence of the overall 4-fold symmetry of the protein and the fact that TM2 is physically close to the symmetry axis. Additional information about accessibility, side chain mobility, and local polarity obtained by SDSL can then be used to test and refine the model.

Intermediate-range (5−20 Å) spin−spin interactions make excellent structural constraints. In both this study and a previous study (*8*), qualitative information about the presence or absence of strong interaction was sufficient to arrive at a model of four α-helices assembled around a central pore. In a channel with 4-fold symmetry, spin−spin interactions can be detected by comparing the EPR spectrum of the channel containing, on average, one or fewer spin labels per tetramer

[3] A_{zz} of spin label **I** was determined in different solvents for comparison: 3:1 (v/v) water:glycerol at −45 °C, 36.2 G; ethanol at −130 °C, 33.9 G; mineral oil at −97 °C, 32 G. These solvents were chosen because they form glasses at low temperature rather than crystalline states (*34*). The approximate dielectric constants for these solvents are (at room temperature) water, 80; glycerol, 43; ethanol, 24; and mineral oil, 2.

to that of a channel containing more than one per tetramer. Assuming identical structures in the vicinity of the spin labels, differences between these spectra must reflect spin−spin interaction. However, obtaining the spectrum of the noninteracting state by underlabeling with R1, as was done in an earlier study (*8*), can be problematic for quantitative work. In particular, where the side chains are in close proximity, the presence of multiple nitroxide side chains can lead to a local structure different than that for just one spin label. In this case, the spectrum of the underlabeled protein is not appropriate to represent the noninteracting state. We have attempted to overcome this problem by labeling the protein with a mixture of R1 and the diamagnetic analogue R1′ (Figure 2). This approach should also be useful for determining the EPR spectrum for the noninteracting state in proteins containing spin-labeled cysteines on a single polypeptide in different environments. Currently, such spectra are obtained as the algebraic sum of the spectra of two individually labeled mutants and are compared with the spectra of a double mutant (*36*). However, this requires that three different mutants must be made for each interacting pair. Using a dilute mixture of R1 in R1′, the desired noninteracting spectrum is obtained by labeling one mutant protein containing two cysteines.

Although the basic model in Figure 6B required only qualitative information on spin−spin interaction, it is desirable to quantify the spin−spin interactions to address one particular feature: at what point is the distance between residues minimal? In principle, this also only requires qualitative assessment of the relative strengths of the interaction. However, it can prove difficult to achieve complete labeling of multiple cysteine residues. Spins in strong interaction have broad spectral features and are easily overshadowed by a relatively small population of monolabeled protein. In these cases, such as the SDSL study of KcsA by Perozo et al. (*8*), qualitative assessment of spin interaction strength based on intensities of normalized spectra is inadequate. In these common situations, another approach is needed.

For a tetrameric channel, there could, in principle, be four interacting spin labels. However, the data presented above show that even O_2 and NiEDDA do not have free access to the channel, and it would be difficult to introduce four nitroxide rings in the same region of the pore. Indeed, modeling of the channel based on the crystal structure shows that it is impossible to accommodate more than two R1 residues in the pore without considerable distortion. Also, under our conditions, we find that no more than 50% of the cysteine residues can be labeled in any of the pore mutants. If the distribution were random, about 70% of the species would bear one or two labels. Taken together, these observations suggest that it is reasonable to treat labeled tetramers as a population with one or two spin labels per tetramer.

At low temperatures, in the absence of motion of the spins, the spectra of interacting spin pairs with a variable fraction of monolabeled protein can be simulated by convolution methods (*20*, *21*) to determine the effective interspin distances (see Materials and Methods). The fits to the spectra are acceptable and provide reasonable estimates of the interspin distance (Figure 5B). Alternatively, the semiempirical $d1/d$ ratio method is a qualitative approach to rank relative strengths of spin−spin interaction, even in the presence of a noninteracting component. Both analyses provide the same result, namely, that R1 residues are closest at position 108 and furthest at position 100.

Comparison of the Spin−Spin Interaction Data with the Crystal Structure. The recently reported crystal structure of KcsA (*4*) allows us to critically evaluate the conclusions derived from spin−spin interactions. In general, the overall agreement of the EPR data with the crystal structure is good. For example, residues projecting toward the symmetry axis based on spin−spin interaction are I100R1, F103R1, A108R1, T112R1, V115R1, G116R1, and Q119R1, with A108R1 being the closest. In the crystal structure, the side chains of I100, F103, T107, A108, A111, and V115 contribute directly to the hydrophobic lining of the pore, and R1 residues at T112 and G116 could easily be positioned for spin−spin interaction. The lack of spin−spin interaction at T107R1 could be due to a low level of labeling at that site. It should be noted that a weak spin−spin interaction was observed for R1 at site T107 in a previously published SDSL study of KcsA (*8*). In addition, we observed no interaction at site 111 due to the low labeling yield at that position (Table 1). In the crystal structure, A111 is located approximately at the point of closest approach between helices in the tetramer, and the low reactivity at this site underscores the tight packing in this region of the pore. The closest approach of R1 residues occurs at A108R1, the residue adjacent to A111 in the structure. The overall agreement between the SDSL data and the crystal structure in this region between I100 and V115 suggests that the structure of KcsA is similar in the crystalline state and in the bilayer.

There are, however, notable differences between the crystal structure and the SDSL data at residues E118 and Q119, where the helix crosses the membrane/aqueous interface. Specifically, residues at E118R1 are noninteracting (Figure 5), exposed to a nonpolar environment (Figure 7), and are relatively mobile (Figure 3). These features suggest that E118R1 is located on the outer surface of the helix in the region of the lipid headgroup. In contrast, the crystal structure places E118 directly in the channel lumen. The R1 residues at Q119 show relatively strong interaction (Figure 5), are relatively immobilized (Figure 3), and face a polar environment (Figure 7), all of which indicate that Q119R1 faces the channel lumen. In contrast, the crystal structure places Q119 on the outer surface of the helix. The observed discrepancy may be due to a genuine difference between the crystal and solution structures. Alternatively, it may be a consequence of the carboxyl-terminal truncation required for crystallization or reflect a decrease in the quality of the electron density map at the last residues in the model.

On the other hand, the crystal structure explains an apparent discrepancy in the EPR data. The environment of F103R1, as determined by collision and polarity measurements (Figure 7), is inconsistent with this residue being exposed toward the pore, an interpretation that is mandatory given the spin−spin interaction at this site (Figure 3). In the crystal structure, the $C_\alpha-C_\beta$ bond of F103 points toward the symmetry axis. However, the side chain turns outward, and the aromatic ring is wedged into the space between two adjacent inner helices where it remains close to the symmetry axis but is exposed toward the bilayer. Thus, F103R1 can be positioned in a low-polarity environment but remain close to the symmetry axis, as indicated by the EPR data.

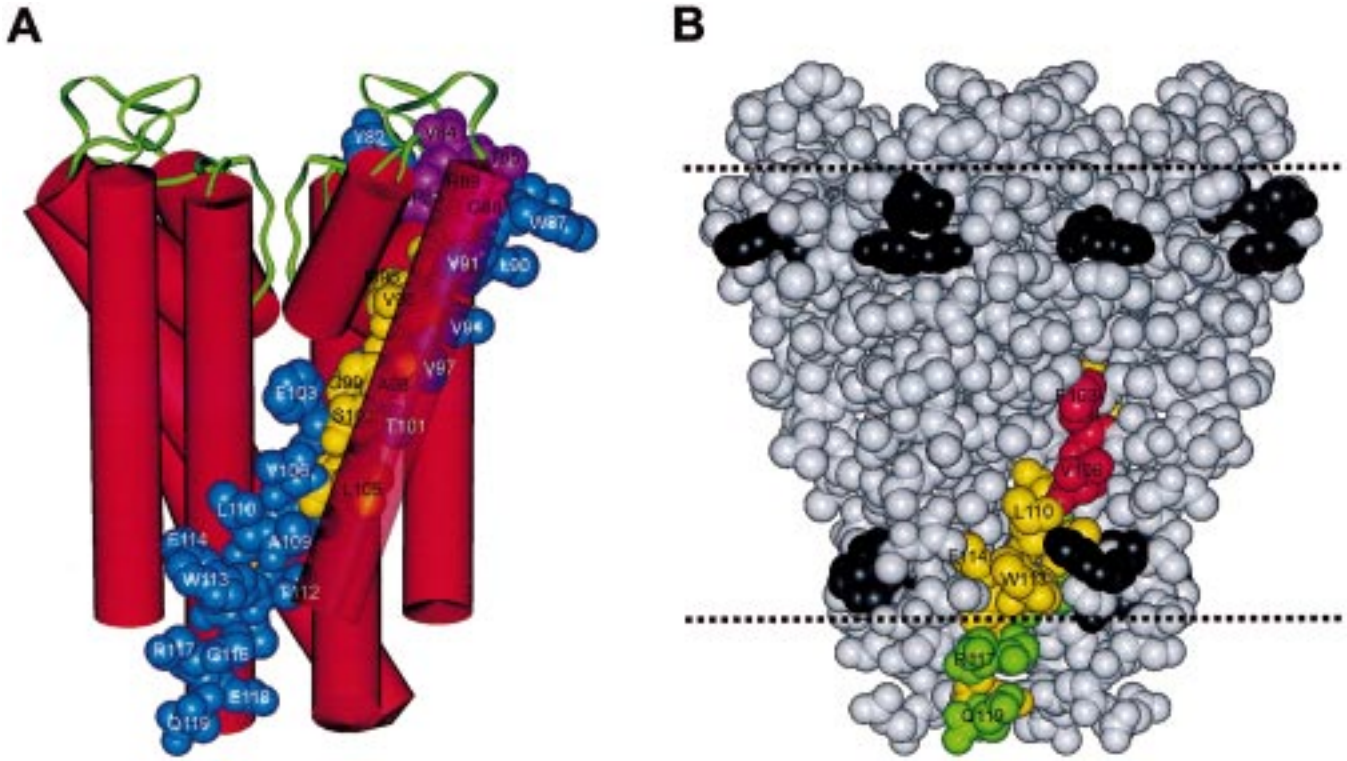

FIGURE 9: Comparison of the results obtained by site-directed spin labeling with the crystal structure. (A) Cylinder representation of the KcsA channel based on the crystal structure, with a TM2 helix (residues 82−119) rendered with space-filling models. Residue 120 was not modeled in the crystal structure. Sites for which cysteine substitution mutants reacted adequately with the spin label are shown in blue, those with essentially background labeling are shown in yellow, and sites for which the cysteine mutants expressed poorly are shown in pink. TM1 of this subunit is rendered semitransparent to allow inspection of the labeled positions. (B) KscA channel rendered with space-filling models indicating the location of residues on the outer surface of the helix, facing lipid or water. The residues in TM2 of one subunit are labeled and color coded according to the local polarity: low polarity (red), intermediate polarity (yellow), and high polarity (green). The remaining aromatic residues are shown in dark gray. The dotted lines approximate the lipid−water interfaces. The lower line is drawn between residues R117 and W113/F114 according to the observed steep decrease of the accessibility to NiEDDA. The upper interface is assumed on the basis of the location of aromatic residues.

Cysteine Reactivity and KcsA Structure. Several sites in TM2 show poor reactivity of the substituted cysteine, particularly in the amino-terminal half of the helix between residues A92 and L105 (Table 1). The TM2 helix in this region is flanked on one side by the pore helix and on the other side by TM1, the outer helix. The residues that label well in this region are all lipid exposed in the crystal structure, such as residues L90, V91, V94, and V97. Indeed, these reactive sites occur periodically in sequence between residues L90 and F103 and lie along the lipid-exposed outer face of the helix (blue residues in Figure 9A). On the other hand, residues buried at protein−protein contacts cannot be labeled above background (yellow residues in Figure 9A). In the sequence from V106 to Q119, all sites reacted with spin label **I** produce spectra uniquely different from background (except A111). The crystal structure shows that these sites are essentially all facing either the channel lumen or the lipid bilayer. Thus, the efficiency of labeling is accurately mirrored in the protein structure, and the sulfhydryl reactivity itself provides useful structural information. In an earlier SDSL study of the KcsA channel, it was reported that all sites in TM2 could be labeled with spin label **I** (*8*). The difference between the results of that study and the present one is unclear. However, the spectra reported in that study for the sites we find to be poorly labeled (e.g., V95, M96, A98, S102, G104, A111) closely resemble the background signal we report here (see Figure 3A).

Interestingly, the extensive studies on T4 lysozyme indicate that even the most buried residues react readily with reagent **I** to produce the R1 side chain (*35*). This result implies that low-frequency thermal fluctuations occur in T4 lysozyme that are of sufficient amplitude to allow access of the reagent to buried sites. Our findings suggest that KcsA is more rigid and that such fluctuations are damped. A potassium channel needs to discriminate between ions whose main difference is size. Maintaining a rigid structure around the selectivity filter, therefore, would be consistent with the function of the protein.

R1 Topography, Mobility, and KcsA Structure. The distinct maxima of the periodic Φ function in Figure 7B identify V106R1, A109R1, and W113R1 as lipid-facing residues. The low polarity found for the environment of R1 at these sites as measured by A_{zz} is consistent with this assignment. Furthermore, the low values of A_{zz} for F103R1 and L110R1 suggest that these two residues also should be included in the lipid-facing set. Figure 9B shows a space-filling model of the KcsA channel based on the crystal structure. It is evident from the structure that sites F103, V106, L110, and W113 are indeed on the outer face of TM2, facing lipid. Residue A109, partly obscured by W26 in the figure, is positioned in a manner that would lead to lipid exposure of an R1 side chain at that site. Thus, Φ and A_{zz} identify a set of TM2 surface residues facing the bilayer that is consistent with the crystal structure. However, the mobility of these

sites is distinctly lower than for lipid-solvated sites on the surface of a transmembrane helix in bacteriorhodopsin or water-solvated sites on helices in T4 lysozyme (Figure 8). This may be due to a combination of factors. For example, the lipid-exposed face of TM2 is located in a cleft on the protein surface formed on one side by TM1 of the same subunit and on the other side by TM2 of the adjacent subunit. The proximity of side chains from these other helices may result in tertiary contacts that serve to immobilize the R1 residue. Alternatively, the relative immobility may be due to an unusually rigid backbone structure in the KcsA channel. The lack of reactivity of cysteine residues located on the surface of TM2 in contact with TM1 is consistent with a rigid structure.

According to the crystal structure, the TM2 helix should be asymmetrically solvated. That is, the surface of the helix facing the symmetry axis should be solvated by water, while the opposing surface should be solvated by lipid. In principle, such asymmetric solvation of helices can be detected by measuring the accessibility of R1 residues along the sequence to a polar (NiEDDA) and hydrophobic (O_2) reagent. Due to the contrasting solubilities of O_2 and NiEDDA in water and lipid, the accessibility parameter should be periodic along the sequence for both reagents but shifted in phase by 180° (*26*, *27*). Unfortunately, this criterion cannot be applied to the KcsA channel, because the helical surface facing the symmetry axis is inaccessible to both O_2 and NiEDDA. The accessibility parameter for a particular reagent is proportional to the product of the local concentration and the diffusion constant. Thus, "inaccessibility" could be due to a low value of either parameter in the lumen, or both, and the data presented here cannot distinguish among these different possibilities. Whatever the reason, accessibility data cannot provide a positive identification of a water-filled lumen in the structure. In the present report, we introduce a novel means of detecting the asymmetric solvation of the helix based on the measurement of local polarity around the R1 side chain. As shown in Figure 7C, the apparent polarity, measured by A_{zz}, is periodic in sequence position in the transmembrane region, oscillating between values expected for bulk water (≈37 G) and lipid (≈32 G). The residues with environmental polarity near that of water face the symmetry axis of the molecule, as identified by spin−spin interaction and the crystal structure. This is a striking result, because the TM2 residues facing the symmetry axis are mostly hydrophobic. Thus, this region appears to be penetrated by water. However, nowhere in the channel lumen does the polarity parameter reach the value expected for bulk water (≈37 G). The largest value of A_{zz} in the channel occurs at T112R1 and is significantly smaller (≈35 G) than the bulk water value, indicating that the water that penetrates the channel does not have bulk water properties. The presence of motionally restricted or ordered water in the channel is consistent with both the low accessibility of NiEDDA to lumen exposed sites and the low mobility of R1 at these sites.

Griffith and co-workers identified a polarity gradient in phospholipid bilayers using the A_{zz} parameter for phospholipids bearing a nitroxide at various positions along the hydrocarbon chain (*34*). The gradient was one of decreasing polarity from the phospholipid headgroup to the bilayer center and was attributed to a gradient in the concentration of water in the bilayer interior. If this is the case, one might expect R1 side chains on the outer surface of a transmembrane helix like TM2 to sense the polarity gradient. Indeed, the data in Figure 7C show that for the lipid-facing R1 residues there is a general trend of decreasing A_{zz}, and hence polarity, as one proceeds from the membrane/water interface (around R117) to the center of the bilayer, near F103 (Figure 9B). The sensitivity of the nitroxide to local polarity may prove useful in the identification of transmembrane helices in membrane proteins of unknown structure, based on the spatial gradient of water concentration and A_{zz} sensed by a nitroxide scan along the helix. In previous work, transmembrane helices were identified on the basis of apparent gradients of [O_2] and [NiEDDA], and hence collision rates, along the bilayer normal (*28*). The measurement of local polarity provides an independent assessment of immersion depth and indicates in the present case that TM2 is a transmembrane helix.

CONCLUSIONS

This study provides the first extensive comparison of structures obtained by EPR and crystallography for a membrane protein. In general, we find that the spin labeling data are in good agreement with the crystal structure reported by Doyle et al. (*4*), demonstrating the applicability of EPR to structure determination in membrane proteins. Using a novel diamagnetic label to aid in the quantification of interspin distances, we present a straightforward model of TM2 assembly based on spin−spin interactions. The EPR constraints for the model were obtained from functional channels reconstituted in phospholipid bilayers, and the good agreement between the techniques indicates that KcsA maintains its overall structure in detergent micelles, although there appear to be significant differences at the lipid−water interface. In addition, the EPR data provide a unique perspective on KcsA structure. The channel appears to be relatively rigid as judged by the poor cysteine reactivity at buried sites and the low mobility of the spin label at lipid exposed sites. The outside surface of the channel experiences a polarity gradient as a function of membrane immersion depth. In contrast, the inside surface, the channel lumen, is in a polar environment despite the hydrophobic nature of its residues. This strongly suggests that the channel is permeated by water.

ACKNOWLEDGMENT

We thank David Sherman for a culture of *S. lividans* and Carole LaBonne for helpful comments on the manuscript.

REFERENCES

1. Schrempf, H., Schmidt, O., Kummerlen, R., Hinnah, S., Muller, D., Betzler, M., Steinkamp, T., and Wagner, R. (1995) *EMBO J. 14*, 5170−5178.
2. Heginbotham, L., Odessey, E., and Miller, C. (1997) *Biochemistry 36*, 10335−10342.
3. Cortes, D. M., and Perozo, E. (1997) *Biochemistry 36*, 10343−10352.
4. Doyle, D. A., Cabral, J. M., Pfuetzner, R. A., Kuo, A., Gulbis, J. M., Cohen, S. L., Chait, B. T., and MacKinnon, R. (1998) *Science 280*, 69−77.
5. MacKinnon, R., Cohen, S. L., Kuo, A., Lee, A., and Chait, B. T. (1998) *Science 280*, 106−109.

6. Tatulian, S. A., Cortes, D. M., and Perozo, E. (1998) *FEBS Lett. 423*, 205−212.
7. le Coutre, J., Kaback, H. R., Patel, C. K., Heginbotham, L., and Miller, C. (1998) *Proc. Natl. Acad. Sci. U.S.A. 95*, 6114−6117.
8. Perozo, E., Cortes, D. M., and Cuello, L. G. (1998) *Nat. Struct. Biol. 5*, 459−469.
9. Li, H. L., Sui, H. X., Ghanshani, S., Lee, S., Walian, P. J., Wu, C. L., Chandy, K. G., and Jap, B. K. (1998) *J. Mol. Biol. 282*, 211−216.
10. Cuello, L. G., Romero, J. G., Cortes, D. M., and Perozo, E. (1998) *Biochemistry 37*, 3229−3236.
11. Heginbotham, L., Kolmakova-Partensky, L., and Miller, C. (1998) *J. Gen. Physiol. 111*, 741−749.
12. Berliner, L. J., Grunwald, J., Hankovszky, H. O., and Hideg, K. (1982) *Anal. Biochem. 119*, 450−455.
13. Sár, P. C., Kálai, T., Bárácz, M. N., Jerkovich, G., and Hideg, K. (1995) *Synth. Commun. 25*, 2929−2940.
14. Green, P. R., and Bell, R. M. (1984) *J. Biol. Chem. 259*, 14688−14694.
15. Gasko, O. D., Knowles, A. F., Shertzer, H. G., Suolinna, E. M., and Racker, E. (1976) *Anal. Biochem. 72*, 57−65.
16. Castle, J. D., and Hubbell, W. L. (1976) *Biochemistry 15*, 4818−4831.
17. Hubbell, W. L., Froncisz, W., and Hyde, J. S. (1987) *Rev. Sci. Instrum. 58*, 1879−1886.
18. Vistnes, A. I., and Puskin, J. S. (1981) *Biochim. Biophys. Acta 644*, 244−250.
19. Altenbach, C., Marti, T., Khorana, H. G., and Hubbell, W. L. (1990) *Science 248*, 1088−1092.
20. Rabenstein, M. D., and Shin, Y. K. (1995) *Proc. Natl. Acad. Sci. U.S.A. 92*, 8239−8243.
21. Steinhoff, H. J., Radzwill, N., Thevis, W., Lenz, V., Brandenburg, D., Antson, A., Dodson, G., and Wollmer, A. (1997) *Biophys. J. 73*, 3287−3298.
22. Pake, G. E. (1948) *J. Chem. Phys. 16*, 327−336.
23. Kokorin, A. I., Zamaraev, K. I., Grigoryan, G. L., Ivanov, V. P., and Rozantzev, E. G. (1972) *Biofizika 17*, 34−41.
24. Hustedt, E. J., Smirnov, A. I., Laub, C. F., Cobb, C. E., and Beth, A. H. (1997) *Biophys. J. 72*, 1861−1877.
25. Heginbotham, L., and MacKinnon, R. (1992) *Neuron 8*, 483−491.
26. Oh, K. J., Zhan, H., Cui, C., Hideg, K., Collier, R. J., and Hubbell, W. L. (1996) *Science 273*, 810−812.
27. Salwinski, L., and Hubbell, W. L. (1999) *Protein Sci. 8*, 562−572.
28. Altenbach, C., Greenhalgh, D. A., Khorana, H. G., and Hubbell, W. L. (1994) *Proc. Natl. Acad. Sci. U.S.A. 91*, 1667−1671.
29. Altenbach, C., Yang, K., Farrens, D. L., Farahbakhsh, Z. T., Khorana, H. G., and Hubbell, W. L. (1996) *Biochemistry 35*, 12470−12478.
30. Deisenhofer, J., and Michel, H. (1989) *Science 245*, 1463−1473.
31. Henderson, R., Baldwin, J. M., Ceska, T. A., Zemlin, F., Beckmann, E., and Downing, K. H. (1990) *J. Mol. Biol. 213*, 899−929.
32. Weiss, M. S., Abele, U., Weckesser, J., Welte, W., Schiltz, E., and Schulz, G. E. (1991) *Science 254*, 1627−1630.
33. Cowan, S. W., Schirmer, T., Rummel, G., Steiert, M., Ghosh, R., Pauptit, R. A., Jansonius, J. N., and Rosenbusch, J. P. (1992) *Nature 358*, 727−733.
34. Griffith, O. H., Dehlinger, P. J., and Van, S. P. (1974) *J. Membr. Biol. 15*, 159−192.
35. Mchaourab, H. S., Lietzow, M. A., Hideg, K., and Hubbell, W. L. (1996) *Biochemistry 35*, 7692−7704.
36. Farrens, D. L., Altenbach, C., Yang, K., Hubbell, W. L., and Khorana, H. G. (1996) *Science 274*, 768−770.

BI990856K